Materials Today Advances 20 (2023) 100433

Contents lists available at ScienceDirect

Materials Today Advances

journal homepage: www.journals.elsevier.com/materials-today-advances/

From unlikely pairings to functional nanocomposites: FeTi–Cu as a model system

Lukas Schweiger [a,*], Daniel Kiener [a], Michael Burtscher [a], Erhard Schafler [b], Gregor Mori [c], Florian Spieckermann [a], Jürgen Eckert [a,d]

[a] Department of Materials Science, Montanuniversität Leoben, Jahnstraße 12, 8700, Leoben, Austria
[b] Physics of Nanostructured Materials, Faculty of Physics, University of Vienna, Boltzmanngasse 5, 1090, Wien, Austria
[c] Chair of General and Analytical Chemistry, Montanuniversität Leoben, Franz Josef-Straße 18, 8700, Leoben, Austria
[d] Erich Schmid Institute of Materials Science, Austrian Academy of Sciences, Jahnstraße 12, 8700, Leoben, Austria

ARTICLE INFO

Keywords:
High-pressure torsion
Nanocomposites
Fragmentation
Process monitoring

ABSTRACT

In order to develop materials for energy storage, a bulk nanocomposite with a composition of FeTi-25 vol% Cu was prepared by high-pressure torsion, with FeTi as functional phase for hydrogen storage and Cu as ductile phase to improve the processability. Despite the use of such a highly ductile auxiliary phase, the processability remained challenging due to strain localization in the softer Cu. This behavior is most pronounced at room temperature, and no nanocomposites were formed. At elevated temperatures, the strong strain rate sensitivity of the flow stress of the nanocrystalline Cu facilitates the formation of a FeTi–Cu nanocomposite due to a self-reinforcing process. Nevertheless, fragmentation of FeTi is limited because the resulting massive strain hardening prevents controlled processing at temperatures <250 °C, and Cu-rich shear bands develop at temperatures >250 °C. Satisfactory microstructural homogeneity is only achieved at the highest deformation temperatures of 550 °C. Overall, this study highlights that for unlikely material pairings, as often required in the pursuit of superior functional materials, the mechanical behavior of the phases involved and their interplay remains critical and must be thoroughly investigated when aiming for controlled structural homogeneity of bulk nanomaterials.

1. Introduction

High-pressure torsion (HPT) allows the preparation of nanocrystalline (nc) bulk and composite materials with improved mechanical and functional properties, e.g., magnetic coercivity or hydrogen absorption [1–6]. The stability of these outstanding properties under harsh environments and over extended periods is essential for future energy applications. Many green technologies require hydrogen, which will become a central energy vector for the upcoming energy transition [7,8]. Hydrogen production [9], utilization [10], and storage [11] are crucial aspects of this transition, with high-performance storage as one cornerstone allowing for simple and ubiquitous use of hydrogen [11–13].

A promising candidate for solid-state hydrogen storage in the form of metal hydrides is intermetallic FeTi [14,15]. While it excels other methods, such as pressurized and liquid hydrogen, in volumetric hydrogen storage capacity, operating conditions, abundance, and price, FeTi has the disadvantage of requiring an activation treatment at high temperatures (400 °C) before hydrogen absorption can take place, and detrimental deactivation occurs when it is exposed to oxygen-containing environments [14–17].

Many studies approach these problems by alloying or mechanical processing, including severe plastic deformation (SPD). Various alloying strategies were addressed [18], and Mn addition showed the most promising results [19]. Other studies focused on improving the absorption properties by SPD, often using ball milling [20–25]. The milled FeTi powders showed good initial absorption behavior, albeit often at reduced absorption capacities.

Abbreviations: HPT, High-pressure torsion; RT, Room temperature; SEM, Scanning electron microscopy; SRS, Strain rate sensitivity; TEM, Transmission electron microscopy; XRD, X-ray diffraction.

* Corresponding author.
E-mail addresses: lukas.schweiger@unileoben.ac.at (L. Schweiger), daniel.kiener@unileoben.ac.at (D. Kiener), michael.burtscher@unileoben.ac.at (M. Burtscher), erhard.schafler@univie.ac.at (E. Schafler), gregor.mori@unileoben.ac.at (G. Mori), florian.spieckermann@unileoben.ac.at (F. Spieckermann), juergen.eckert@unileoben.ac.at (J. Eckert).

https://doi.org/10.1016/j.mtadv.2023.100433
Received 31 July 2023; Received in revised form 4 October 2023; Accepted 8 October 2023

Edalati et al. reported on the processing of FeTi and derivatives by HPT [26,27]. Due to its high hardness and brittle nature, it is, however, difficult to process FeTi, and even HPT results only in a heterogeneous microstructure [26]. A later study showed direct synthesis of FeTi by mechanical alloying using HPT [28]. Such processing routes resulted in enhanced absorption properties as well as enhanced oxygen resistance. However, the capabilities of HPT extend beyond simple mechanical processing and alloying. It is a versatile tool for preparing complex multi-phase materials and composites with enhanced mechanical and functional properties. The resulting materials can be nanocomposites [29], supersaturated solid solutions [30], or thermodynamically stable phases, but also otherwise inaccessible and metastable phases can be obtained [31].

A promising route is to blend different powders and compact and deform them using HPT. Multiple material systems have been investigated following this strategy, many of which contain Cu, as this material exhibits excellent ductility and deformability, e.g., Cu–W [32,33], Cu-Cr [34], Cu-Co [35], and Cu–Ag [36,37].

Although some reports exist on the processing and mechanical alloying of FeTi by HPT [26,27,38,39], no studies are available on preparing nanocomposites containing FeTi. Such nanocomposites could exhibit unexpected phases, microstructure, and properties. Furthermore, they could be starting points for further processing, for example, the preparation of nanoporous materials with significantly increased surface area, such as previously realized for Cu–W [40], Cu-Fe [41], Au-Fe [42], and Cu–Ag–Fe [43].

Processing functional materials with specific functional properties as the primary focus can be tedious because the associated mechanical properties are often poor. This is also the case with the hard and brittle FeTi phase. Controlled processing is, however, key to precisely tuning the material structure and properties. Therefore, in this work, we opt to circumvent the limited bulk processability of FeTi by deforming it with Cu, preparing a homogeneous FeTi–Cu nanocomposite. Cu takes the role of a ductile phase to improve deformability. The Cu content was reduced as much as possible to ensure the highest amount of the active phase FeTi while maintaining a percolating structure [44]. Percolation will be a crucial requirement for any later formation of nanoporous structures. Therefore, we used an optimized Cu content of 25 vol%.

Starting from powders, an FeTi-25 vol% Cu nanocomposite was successfully prepared using optimized HPT processing. It is found that localization in the softer Cu phase hinders uniform grain refinement of FeTi. It is crucial to increase the deformation temperature to obtain a nanocrystalline composite. We propose that the temperature and grain size dependent strain-rate sensitivity (SRS) of Cu is the origin of the far-improved refinement behavior of the composite at elevated temperatures. In addition, mechanical alloying stabilizes a more uniform deformation. Despite this, Cu-rich shear bands remain present even at the highest deformation temperatures. The process knowledge gained in this work is valuable for highlighting possible routes around the associated difficulties when processing unlikely material pairings.

2. Methods

We synthesized FeTi by arc melting (Arc Melter AM 0.5, Edmund Bühler GmbH, Germany) from stoichiometric quantities of Fe (flakes, 99.99+ %, HMW Hauner GmbH, Germany) and Ti (granules, 99.995%, HMW Hauner GmbH, Germany). The ingots were remelted five times to ensure homogeneity and crushed afterward using mortar and pestle. The crushed FeTi and Cu powders (99.9%, Alfa Aesar, US) were intimately mixed by ball milling (Planetary ball mill PM 400, Retsch GmbH, Germany). The powders were weighted (ensuring 25 vol% Cu, i.e., 43 at.% and 31 wt% Cu) and sealed in a steel milling vial (50 ml volume) with 20 steel balls (10 mm diameter) in a glovebox under Ar atmosphere (H_2O < 0.5 ppm, O_2 < 0.5 ppm). The ball-to-powder ratio was 10:1. This pre-milling was performed for 1 h at 300 rpm. The vial was transferred and opened in a glove box to minimize oxygen contamination. The resulting FeTi–Cu powder did not separate into the elemental powders and provided good handleability.

Subsequently, the FeTi–Cu powder was consolidated in a custom-made HPT device under an Ar-atmosphere using an inert gas holder, as reported previously [45]. A Cu-ring was glued on top of the cavity to minimize spilling [45]. The tool steel anvils for compaction had a cavity with a diameter of 8 mm and a depth of 0.3 mm. A pressure of 7.5 GPa and 1/8 revolution was applied to ensure complete compaction and minimal porosity. The resulting pellets had a diameter of 8 mm, a thickness of about 1.1 mm and were handled in ambient atmosphere. Both anvils and compacted samples were sandblasted before HPT processing to ensure sufficient friction and avoid slipping during deformation. The anvils for deformation had a cavity with a diameter of 8 mm and a depth of 0.15 mm. The compacts were then deformed by HPT for 10, 50, and 100 revolutions at room temperature (RT), 200 °C, 400 °C, and 550 °C, respectively. The applied pressure was 7.5 GPa for RT and 200 °C and 6 GPa for 400 °C and 550 °C. The rotation speed was 1 rpm. During RT deformation, the anvils were additionally cooled with pressurized air to minimize heating effects due to the severe deformation applied. For selected specimens, the torque was measured during HPT processing [46]. At elevated temperatures, the measurement time was restricted because of possible damage from the temperature rise. The shear strain γ at a specific radius r introduced during HPT deformation was estimated based on the expression [47]:

$$\gamma = \frac{2\,\pi\,n\,r}{t} \tag{1}$$

with n being the number of revolutions and t the thickness of the sample. After HPT deformation, the samples had a thickness of about 0.5 mm. From the torque T, the shear stress τ was calculated using the equation [46]:

$$\tau = \frac{3T}{2\pi r^3}. \tag{2}$$

To identify the phases and to quantify defect densities and mechanical alloying, synchrotron X-ray diffraction (XRD) was performed on the P02.1 Powder Diffraction and Total Scattering Beamline of PETRA III (DESY Hamburg) in transmission geometry with a Varex XRD 4343CT (150 × 150 μm^2 pixel size, 2880 × 2880 pixel area) detector and a photon energy of 60 keV. The diffraction patterns were calibrated using a CeO_2 reference and the pyFAI software [48]. The beam was positioned to coincide with a radius of 3 mm of the respective HPT disks. The broadening of reflections can be traced back to many structural defects, including grain boundaries (i.e., crystallite size), microstrains, dislocations, stacking faults, and more [49]. To discriminate the broadening originating from grain size and dislocations, the diffractograms were evaluated using the Williamson-Hall [50] and modified Williamson-Hall [51] methods using a Python 3.9 script including libraries such as lmfit [52] (version 1.0.3) and Scipy [53] (version 1.6.2). The latter also considers anisotropic broadening due to dislocations employing contrast factors, yielding more accurate results. Therefore, the modified-Williamson-Hall method proved more reliable, and this data was used for further interpretation. Full profile fitting was considered inadequate for XRD evaluation since the patterns contained only a few non-overlapping, independent peaks. The dislocation density ρ was calculated using equation [51]:

$$\rho = \frac{\pi A b^2}{2} k \tag{3}$$

with k being the slope in the modified Williamson-Hall fit and b the Burgers vector. The constant A is set to 1, which constitutes the upper bound of the microstrain-based dislocation density [54].

The HPT disks were cut in half for microstructural investigations to obtain complete cross-sections. The structure and morphology of the polished cross-sections were investigated by scanning electron

microscopy (SEM; LEO type 1525, Carl Zeiss GmbH, Germany). Transmission electron microscopy (TEM) images were recorded at a cross-sectional view in scanning TEM (STEM) mode utilizing a JEM-2200FS microscope, JEOL Ltd., Japan. The preparation steps for achieving electron transparent specimens included polishing, dimple grinding, and final ion-milling of the disks at a radius of 3 mm. For parameterization (area fractions, particle analysis), the software packages Ilastik [55] (Version 1.3.3), Fiji (Version 1.53) [56] (including the BioVoxxel plugin [57]), as well as a Python 3.9 script including packages such as Scipy [53] (version 1.6.2), Scikit-Image [58] (Version 0.18.1) and OpenCV [59] (Version 4.5.4.58) were employed.

The Vickers microhardness was measured on the polished cross-sections previously prepared for SEM investigations using a universal laboratory hardness tester (DuraScan, ZwickRoell GmbH, Germany).

3. Results

Backscattered electron (BSE) micrographs of the composites deformed at different temperatures are shown in Fig. 1; all images were taken after 50 revolutions at $r = 3$ mm ($\gamma \approx 1900$) in the tangential direction of the HPT disk. The main feature evident at low magnifications is relatively large FeTi particles (dark phase). Such particles significantly exceeding the targeted nanocrystalline/ultra-fine-grained length scale, i.e., having a diameter larger than 500 nm, are referred to as residual FeTi particles from now on and were identified under all processing conditions.

The most heterogeneous microstructure of all studied samples is found for RT deformation, with large FeTi particles embedded in a Cu-matrix. As seen in Fig. 1 (a)–(c), some refinement of FeTi takes place. However, most grains are still in a micrometer or ultra-fine-grained (ufg) regime, indicating insufficient fragmentation and deformation of the FeTi phase. The microstructures obtained after processing at 200 °C and 400 °C are displayed in Fig. 1 (d)–(i). At 550 °C, the microstructural homogeneity improves markedly, and the amount of residual FeTi is minimal; only a few large FeTi particles remain.

All samples deformed at elevated temperatures (>200 °C) form nanocomposites, as shown in Fig. 1 (f), (i), and (l). These nanocomposites constitute the matrix in which residual FeTi particles are embedded. The micrographs also confirm that the nanocomposite grain size depends on the deformation temperature and increases with temperature. The presence of residual FeTi, albeit less severe than in case of RT deformation, is again associated with insufficient and inhomogeneous refinement.

Depending on the exact conditions, we observed another micro- to nanoscale feature. During deformation at 200 °C, a homogeneous nanocomposite forms, while at 400 °C and 550 °C, bright bands, marked by arrows in Fig. 1, are visible. Due to the bright contrast, these bands must contain higher atomic number elements and are identified as Cu-rich regions. The orientation of the bands varies with the radial position, but generally, they are parallel or slightly inclined to the shear plane. These bands are also commonly observed close to residual FeTi grains and become more pronounced as deformation progresses.

The microstructural homogeneity was quantified by determining the area fraction of residual FeTi across the entire cross-section using image analysis and plotting it against the number of revolutions n and applied shear strain γ in Fig. 2 (a). As FeTi is refined below a certain limit (<0.5 μm for area analysis; <1 μm for particle analysis), i.e., to the ufg and targeted nanocrystalline regime, it was not counted anymore. FeTi particles close to the 0.5 μm threshold are associated with a larger uncertainty in this analysis, but their relative contribution to the area fractions is comparably small. Still, it should be kept in mind that numerous of those particles exist and are only observable in high-resolution SEM micrographs, as seen in Fig. 1. As shown in Fig. 2 (a), under most conditions, microstructural refinement arrives at a limit at which further deformation does not yield any reduction of residual FeTi. This limit varies with deformation temperature. At RT, there is little refinement, and a steady state is reached after only ten turns. More refinement occurs at 200 and 400 °C, where a steady state is observed after 25–50 revolutions. For samples deformed at 550 °C, there is no limit to the structural refinement, and the microstructure is well homogenized after 50 revolutions.

The microstructure was further parameterized by determining the

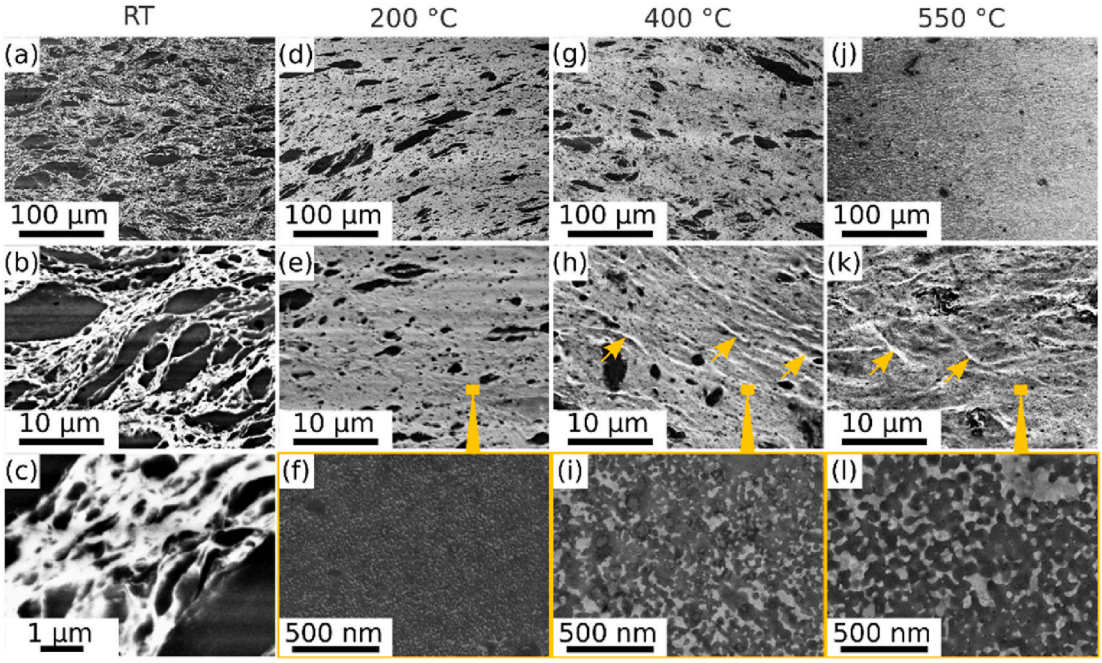

Fig. 1. The SEM micrographs show HPT samples subjected to 50 revolutions ($r = 3$ mm, $\gamma \approx 1900$) at (a)–(c) RT, (d)–(f) 200 °C, (g)–(i) 400 °C and (j)–(l) 550 °C. The brighter phase corresponds to Cu and the FeTi–Cu nanocomposite, respectively, while the dark phase is residual FeTi. Cu-rich shear bands are highlighted by yellow arrows. Images (f), (i), and (l) were taken with an In-Lens detector, all others with a BSE detector. (For interpretation of the references to color in this figure legend, the reader is referred to the Web version of this article.)

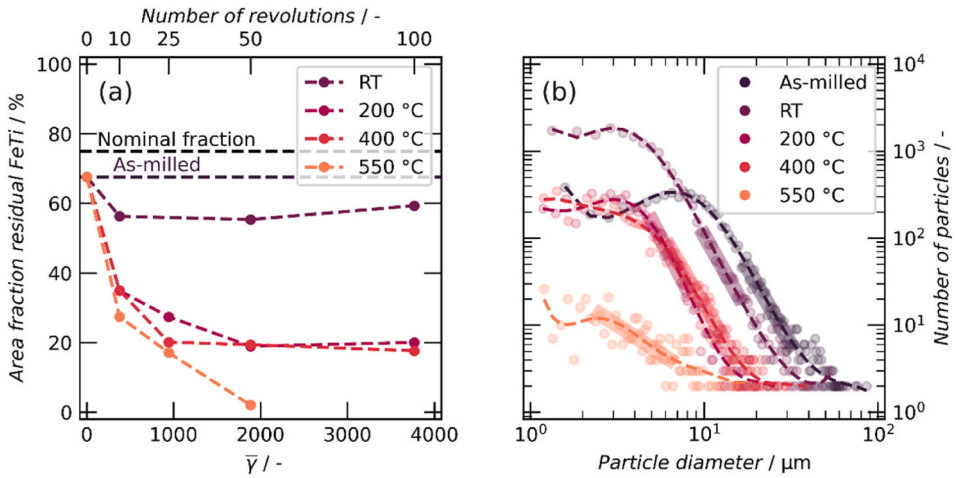

Fig. 2. (a) Area fraction of residual FeTi particles embedded in the Cu/FeTi–Cu matrix over the whole cross-section as a function of strain at $r = 3$ mm. (b) Particle size distribution of residual FeTi particles in samples deformed for 50 revolutions at a radius between 3.5 mm and 1.5 mm ($\gamma \approx 950$–2200) plotted in a double-logarithmic fashion. Splines are added as guides to the eye. Linear fits for the determination of the fractal dimensions are also given.

number and size distribution of residual FeTi particles in cross-sections from radial positions within 1.5–3.5 mm for samples deformed for 50 revolutions ($\gamma \approx 950$–2200). The results are plotted in Fig. 2 (b). The lower tail of the distribution is not resolved, but the curve agrees well with a fractal distribution, having a linear slope in the double logarithmic plot [60]. A linear fit in this regime yields the associated fractal dimensions, being between 3.3 and 4 for RT to 400 °C and significantly lower, 1.3 for 550 °C; for more details, refer to Table S1. Overall, the trends observed in Fig. 2 (a) are confirmed, i.e., the number and size of residual FeTi particles are reduced as temperature increases but stay constant in the range of 200 °C–400 °C. Additionally, this representation highlights that the whole particle distribution shifts to smaller sizes for these intermediate temperatures, suggesting uniformly increased refinement. The drastic enhancement of homogeneity at 550 °C is mainly associated with a superior refinement of already smaller FeTi grains, while the particle size distributions converge at larger particle diameters. Consequently, deformation at 550 °C leads to the best homogeneity, but a few large FeTi particles remain in the microstructure.

High-resolution SEM images, as depicted in Fig. 1 (f), (i), and (l), discriminate between the apparent phases; however, they do not resolve the individual grains. TEM investigations were performed to access the latter. The corresponding BF-STEM images, including the normalized grain size distributions, are provided in Fig. 3. However, the Cu and FeTi grains cannot be distinguished based on these images. Therefore, the grain size distributions in Fig. 3 (d) represent the combined FeTi and Cu distributions. Nevertheless, the general trend is for grain sizes to increase with higher deformation temperatures, in agreement with the SEM and TEM results.

Synchrotron X-ray diffraction was used for structural characterization with high sensitivity for crystallographic phase constitution and phase-specific grain sizes and defect densities. The diffractograms shown in Fig. 4 (a) confirm that FeTi and Cu are the main constituting phases for all processing conditions. Only minor amounts of the Fe_2Ti phase are detected in the samples deformed at 550 °C, as highlighted in Fig. 4 (b).

The positions of the reflections shift slightly with deformation temperature, and the associated changes in lattice constants are plotted in Fig. 4 (c). Well-separated reflections, listed in Table S2, were used to

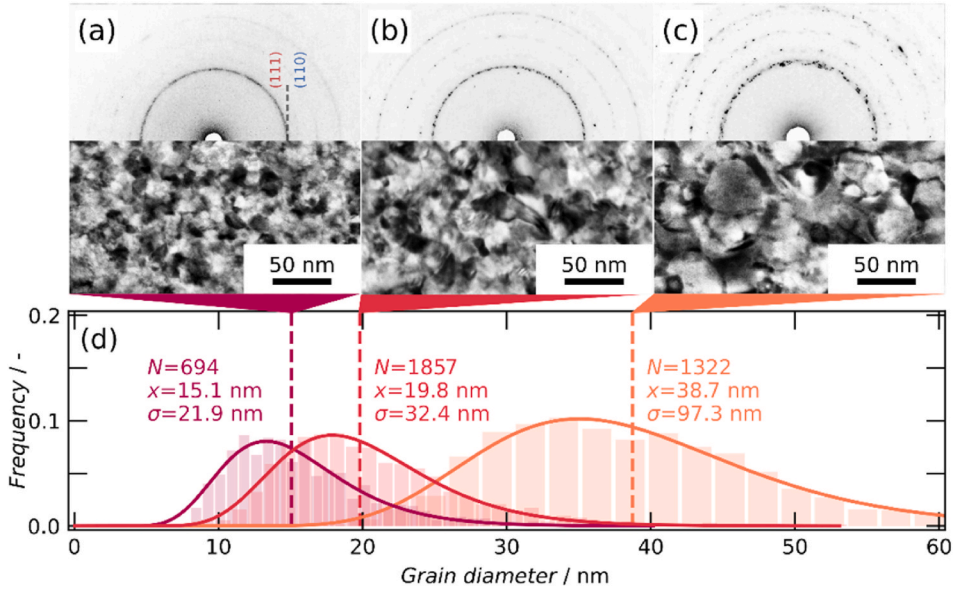

Fig. 3. Cross-sectional TEM micrographs and SAED patterns taken at a radius of 3 mm of samples deformed for 50 revolutions ($\gamma \approx 1900$) at (a) 200 °C, (b) 400 °C and (c) 550 °C and (d) associated probability density distributions.

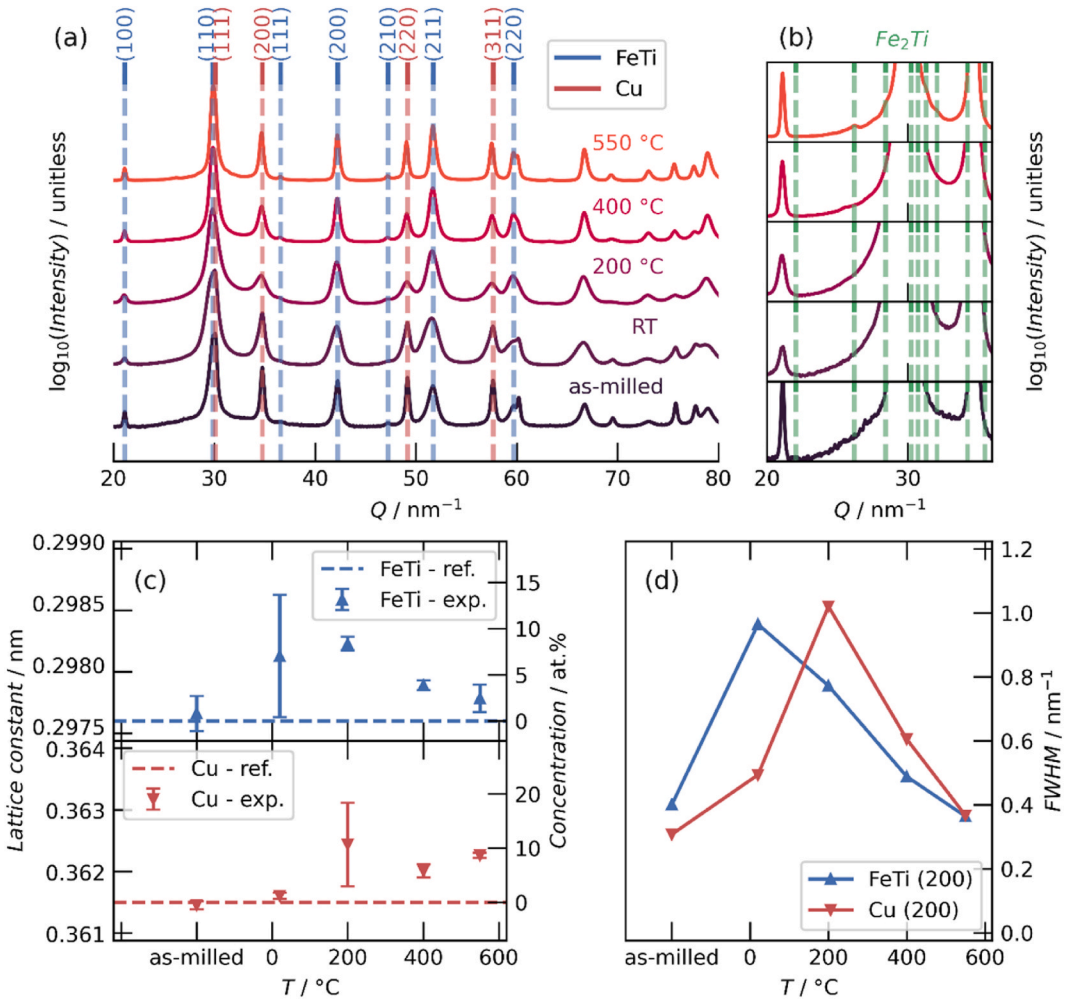

Fig. 4. (a) Synchrotron XRD measurements of samples deformed for 50 revolutions ($r = 3$ mm, $\gamma \approx 1900$) at various temperatures. Note the logarithmic scaling of the intensity. (b) The magnified region of the pattern highlights the formation of minor amounts of Fe_2Ti at high temperature HPT deformation. (c) Lattice parameters and atomic concentrations are calculated from the reflections given in Table S2 and (d) *FWHM* of the (200) peaks of FeTi and Cu as a function of the processing deformation temperature.

minimize errors due to overlap. The expansion of the lattice constants observed for both phases is taken as an indicator for mechanical alloying, and based on literature [61,62], the atomic concentrations were estimated. Mechanical alloying of Cu becomes more pronounced with increasing temperature, while FeTi has a distinct maximum at 200 °C, with a concentration of about 8 at.% Cu, after which the lattice constant approaches again the value of unalloyed FeTi. It should be noted that for Cu, an approximation was to calculate only the average Fe + Ti concentration based on an average lattice expansion due to alloying with both species, i.e., 8 at.% is equivalent to 4 at.% Fe plus 4 at.% Ti. The patterns with the broadest peaks, i.e., RT for FeTi and 200 °C for Cu, coincide with a significant standard deviation in the lattice constant, likely due to increased uncertainties in determining the exact position. The two-phase composite structure is maintained at all conditions and no single-phase supersaturated solid solution forms.

All patterns exhibit broad peaks, indicating the material's highly defective and fine-grained state after SPD. As Fig. 4 (d) depicts for exemplary peaks, peak broadening reaches a maximum at RT and 200 °C for FeTi and Cu, respectively. At higher deformation temperatures, the full-width-at-half-maximum (*FWHM*) decreases again. Based on this broadening, the coherent scattering domain (CSD) sizes and the microstrain-based dislocation (ρ) densities were determined. The FeTi and Cu phases yield good fits using the modified Williamson-Hall procedure [51]. This modified variant considers anisotropic broadening and is especially well-suited for highly dislocated crystals. When applied, a significantly better fit could be obtained in the case of Cu. The improved fit quality indicates that Cu contains many dislocations, a significant contributor to (anisotropic) peak broadening.

The obtained CSD sizes are plotted together with the results from TEM in Fig. 5. The TEM values, representing the combined grain sizes of FeTi and Cu, align perfectly with CSD sizes. Altogether, the results from TEM and XRD agree well and confirm the nanocrystalline (<100 nm) nature of the FeTi–Cu composite material at all processing conditions. The dislocation densities evaluated from XRD are included in Fig. 5. These decrease at elevated temperatures, especially for FeTi, due to recovery phenomena.

The mechanical properties were evaluated by Vickers microhardness $HV_{0.5}$ measurements as a function of radius and, therefore, the strain applied on the microstructure. The indentation area contained the respective matrix phase and residual FeTi, yielding an average composite microhardness (Cu, FeTi–Cu nanocomposite, and residual FeTi). The results are plotted in Fig. 6 (a). The measurements indicate hardness saturation after a certain degree of deformation. This is observed for many HPT-deformed single and multi-phase material systems [30, 63–65]. Based on the notion that microhardness is a well-suited descriptor for microstructural evolution, a detailed investigation of the hardness as a function of radial position within the HPT disk is represented in Fig. 7.

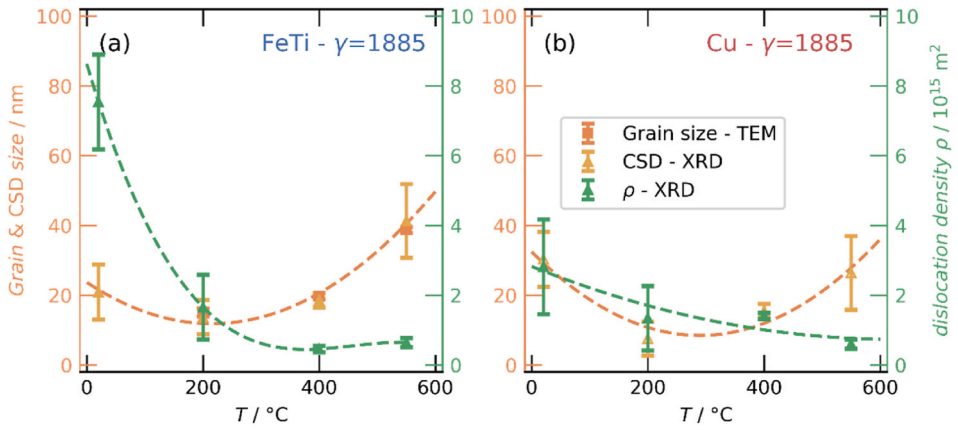

Fig. 5. (a) FeTi and (b) Cu grain/CSD size as a function of processing temperature as obtained by TEM and XRD (modified Williamson-Hall). The dislocation densities ρ, as obtained by XRD, are included. Dashed lines act as guides to the eye. The data are from samples HPT deformed for 50 revolutions and taken at $r = 3$ mm ($\gamma \approx 1900$).

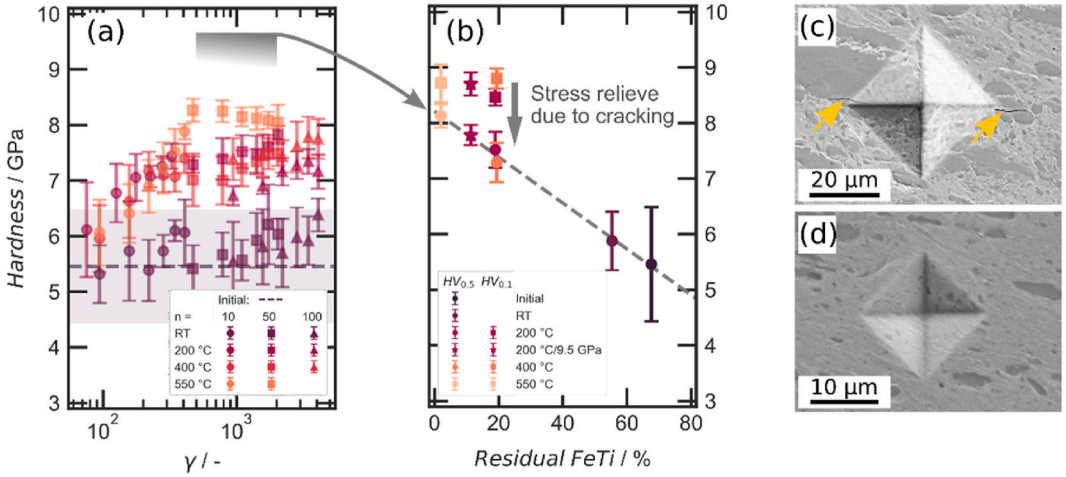

Fig. 6. (a) Evolution of microhardness of the composites with increasing deformation strain. The microhardness plus standard deviation is included as a purple band for the compacted powder. (b) Average microhardness when strained between $\gamma \approx 630$–2200 plotted (a grey region in (a)) against the area fraction of residual FeTi. Indentation was done randomly ($HV_{0.5}$) and selectively in the nanocomposite matrix ($HV_{0.1}$). SEM images highlight the differences when indenting with (c) high loads ($HV_{0.5}$) and (d) low ($HV_{0.1}$); cracking is indicated by yellow arrows in (c). (For interpretation of the references to color in this figure legend, the reader is referred to the Web version of this article.)

Fig. 6 (a) shows that RT deformation does not result in significant strain hardening compared to the compacted samples. Interestingly, from the box plots of the individual samples in Fig. 7, it becomes apparent that some hardening does occur, but it is localized at the edge of the HPT disk, irrespective of the applied strain. The reasons could be the different stress states close to the disk edge.

Samples deformed at elevated temperatures exhibit microstructural refinement and saturation behavior. Saturation is seen in Fig. 6 (a) as a hardness plateau, which evolves at $\gamma \approx 300$ for 200 °C and 400 °C, at $\gamma \approx 500$ for 550 °C. This indicates that further deformation does not result in further refinement, despite the heterogeneous microstructure and the presence of residual FeTi. The hardness level of the plateau depends on processing temperature, whereby 200 °C and 400 °C yield a hardness level of ≈ 7.5 GPa, while for 550 °C, a level of ≈ 8 GPa was achieved. The same saturation behavior is also visible for individual samples in Fig. 7. At elevated deformation temperatures, all samples exhibit a distinct rise in hardness with radius at low strains, while at higher strains, it does not change within the error margins. It also becomes apparent that the samples deformed at 550 °C for 50 revolutions exhibit the narrowest and most uniform hardness distribution, in agreement with a high degree of homogeneity.

The Vickers microhardness in the saturation regime, as plotted in Fig. 6 (b), correlates with the amount of residual FeTi, one of the main features of the composite microstructure. The hardness was taken from the sample deformed for 50 revolutions and from a radial range of 1–3.5 mm corresponding to $\gamma \approx 630$–2200. As the number of residual FeTi particles decreases with higher deformation temperatures, the hardness of the composite increases due to Hall-Petch strengthening accompanying the improved refinement of both phases. For most indents, however, cracks are observed, being more severe for the heterogeneous samples, as depicted in Fig. 6 (c). This results in stress relief and lowering of the hardness. Therefore, the $HV_{0.5}$ hardness should rather be interpreted as a measure of microstructural homogeneity and saturation than as the hardness of the nanocomposite matrix. This view is supported by the scaling of the standard deviation with the residual FeTi content, exhibiting a large value of about 1 GPa for the more heterogeneous microstructure at RT and about 0.2 GPa for the more homogeneous nanocomposites at elevated temperatures.

Selective indentation at lower loads ($HV_{0.1}$) was carried out to obtain the hardness of the nanocomposite matrix and to avoid the cracking mentioned above. The nanocomposite matrix yields hardnesses exceeding the previous $HV_{0.5}$ values, as evident in Fig. 6 (b). Such a load-

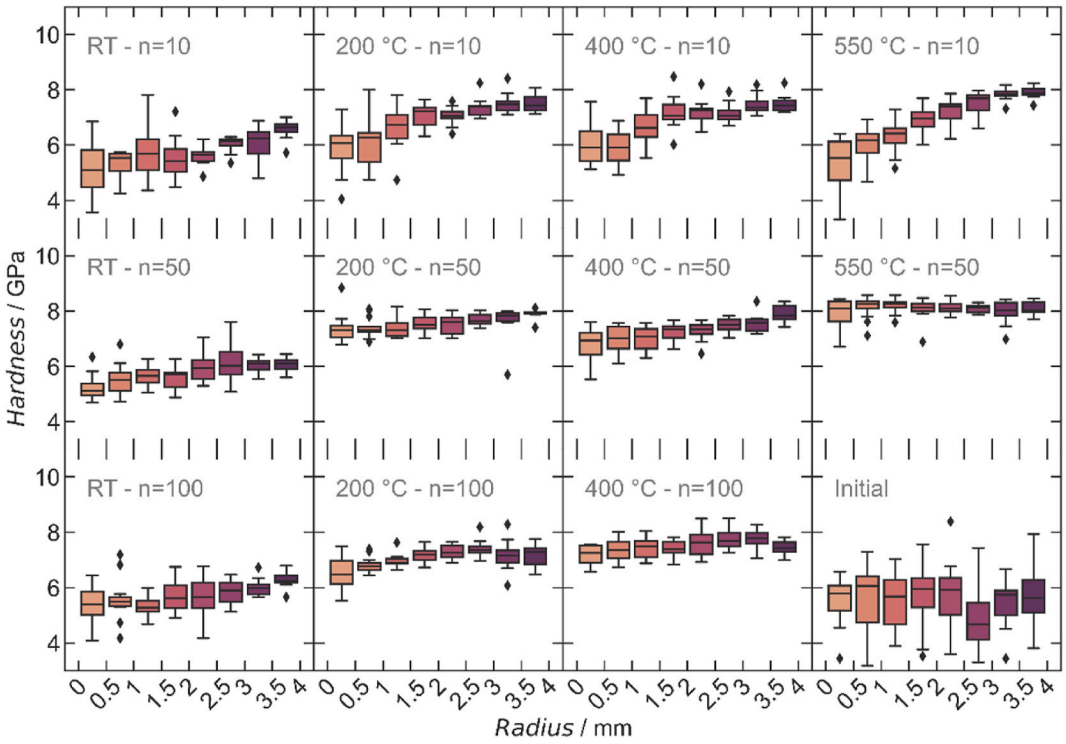

Fig. 7. Boxplot of the hardness ($HV_{0.5}$) as a function of radius for samples deformed at different temperatures and to various numbers of revolutions *n*. The black checks (◆) indicate outliers.

dependent behavior can be related to an increasing elastic deformation component at lower loads or to crack formation at higher loads, leading to stress relief and lower hardness [66,67]. As Fig. 6 (d) and Fig. S1 confirm, lower loads do not result in appreciable cracking. The increasing differences in $HV_{0.5}$ and $HV_{0.1}$ values at lower deformation temperatures cannot be explained solely by elastic deformation and must thus be related to cracking at the indent. Consequently, the $HV_{0.1}$ values can be regarded as being closer to the actual hardness of the nanocomposites at the expense of losing information about microstructural heterogeneity and saturation behavior. However, these values might slightly overestimate the actual value due to significant elastic deformation.

Finally, to better understand the mechanisms controlling refinement, the torque required to deform the material was used to construct the flow curves in Fig. 8. Under all conditions, the curves show a substantial increase in shear stress as deformation starts. After this initial increase,

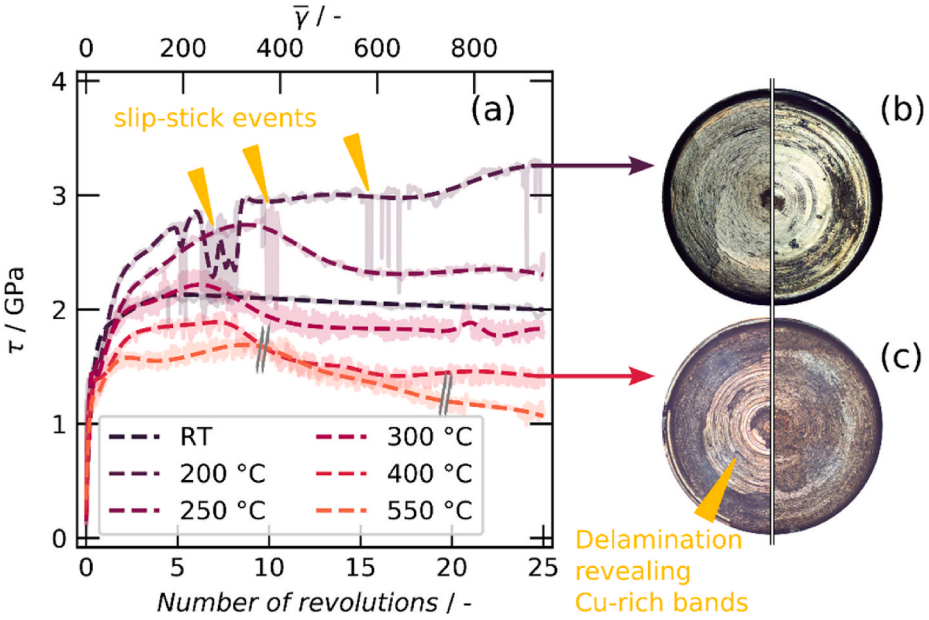

Fig. 8. (a) Flow curves obtained by torque measurements during HPT processing. Yellow arrows mark slip-stick events. The average strain state of the sample is given at the top; this is equivalent to the strain at $r = 3$. Sample surface of samples deformed at (b) 200 °C and (c) 400 °C. (For interpretation of the references to color in this figure legend, the reader is referred to the Web version of this article.)

the temperature has a marked effect on the deformation behavior. At RT, the shear stress reaches a maximum of about 2.1 GPa, followed by a minor but steady decline. At 200 °C, the curve increases to the highest shear stress of up to 3 GPa. At this level, sudden stress drops occur regularly. Each event is associated with loud noises the HPT emits during deformation. Above 250 °C, the curve arrives at a distinct temperature-dependent maximum, followed by a decline and a steady state. This steady state behavior is less pronounced at 550 °C than at 300 °C and 400 °C. The latter results must be interpreted carefully, as the torque could not be measured at such high temperatures over extended periods for instrumental reasons. Thus, grey marks indicate the breaks required for cooling the device. As seen in Fig. 8 (b) and (c), after deformation at 200 °C, the sample surface is smooth, while at 400 °C, it is rough with delaminated regions showing Cu-rich regions.

4. Discussion

The results show significant differences between the composite's refinement behavior at RT and elevated temperatures. The following section discusses the reasons for the absence of a homogeneous nanocomposite at RT, followed by the phenomena allowing its formation at elevated temperatures. These findings will be combined to rationalize the complex micro- and nanostructure of the FeTi–Cu material.

4.1. Insufficient refinement at room temperature

HPT deformation at RT does not result in the formation of a uniform nanocomposite. Instead, as Fig. 1 (a)–(c) show, the microstructure consists of fractured FeTi particles, ranging from the nanocrystalline to the microcrystalline regime, embedded in a Cu matrix. Fig. 2 (a) reveals that FeTi particles are broken up at low strains, but a steady state is soon reached, and the amount of residual FeTi remains constant. The particle distribution, plotted in Fig. 2 (b), shifts to smaller particle sizes than the initial state, indicating uniform but little refinement across the whole size range.

Therefore, as apparent in Fig. 6, no microstructural saturation and no increased hardness plateau are reached. The slight hardness increase with radius in Fig. 7 might originate from the different, more complex stress states present close to the edge of the HPT disk. The absence of saturation indicates insufficient refinement, either due to deformation localization or slipping of the sample in the anvils.

These possibilities can be discriminated based on the flow curves in Fig. 8. An increase in torque can be related to strengthening, but also lateral material flow, a reduction to softening of the material [46,68–71]. Instantaneous drops in shear stress can be associated with slip-stick events, in which the friction between the sample and the anvil is insufficient to introduce more strain [72]. As RT deformation starts, the shear stress initially increases, followed by a slight but continuous drop. Together with microstructural investigations, this implies that refinement and the associated strain hardening halts, and the composite locally deforms in one of the constituent phases. Such localization originates from the strength differences of the respective phases. The hardness of bulk Cu subjected to SPD is 1–2 GPa [73–75], and can reach up to 3 GPa for nc-Cu [76]. Annealed FeTi has a hardness of 3.5 GPa, 5.5 GPa when prepared by mechanical alloying [77], and up to 10 GPa after HPT [26]. As the initial powder was ball milled, initial hardness values of 2 GPa [74] and 5 GPa [77] for Cu and FeTi are anticipated. This strength difference supports initial deformation localization in the softer Cu phase, while the harder FeTi phase will refine by fracture. A similar behavior has been observed for other soft-hard metallic composites [30], e.g., Cu–W [32,33], Cu-Cr [34], Cu-Co [35], and Ni–Ag [78] composites. In many material systems, the strength of the individual phases converges, e.g., in the Cu–Co system [35]. On the one hand, such convergence of the mechanical strength of the individual phases, often accomplished by strain hardening of the softer phase, is important for efficient refinement, either by fragmentation or co-deformation. On the other hand, many hard-hard contact points should be present at high volume fractions of the stronger phase, necessitating deformation of it too. For FeTi–Cu at RT, neither is the case; strain hardening of Cu and FeTi–FeTi contacts is insufficient, and localization in the Cu phase persists. Fig. 5 highlights that despite the massive strain introduced in the Cu phase, its dislocation density/CSD size remains below/above that of FeTi. High dislocation densities/small CSDs are associated with a high-strength state, which qualitatively confirms the strength difference between FeTi and Cu. While in the ufg-Cu dislocations are dynamically consumed during the severe deformation process [79,80], in the mostly undeformed FeTi particles their concentration remains significantly higher. Consequently, HPT deformation at RT results in insufficient refinement due to deformation localization caused by the persisting strength difference between the constituent phases of the composite.

4.2. Nanocomposite formation at elevated temperatures

Despite the initial differences in strength and deformation localization, an FeTi–Cu nanocomposite is formed at elevated temperatures, as clearly observable in Fig. 1. Three possible phenomena can explain such microstructural evolution: (i) Strength convergence, (ii) mechanical alloying, and (iii) suppression of localization.

(i) Convergence of strength

As strength difference is the reason for insufficient refinement at RT, it might be obvious that this discrepancy must be reduced at higher temperatures. Otherwise, deformation localizes in the softer phase, and the stronger particles cannot fracture and refine. Indeed, the intrinsic mechanical properties of the constituent phases should converge, as fcc Cu should be affected to a lower extent by temperature than FeTi with a B2 structure [81–83]. For Cu, a gradual but small decrease in flow stress ratio was observed up to about 500–600 °C; this decrease is less pronounced at higher strain rates [84], such as during HPT. For FeTi, the Vickers microhardness steadily decreases from around 200 °C upwards; ductile deformation behavior concomitant with a strongly reduced yield strength occurs above 500 °C [85,86]. The latter behavior resembles a brittle-to-ductile transition, as reported for other B2 intermetallic materials, such as FeAl [87] or TiAl [88].

These trends point towards reduced strength differences at elevated temperatures between the constituent phases, but whether this is enough to converge fully remains questionable. The large residual FeTi particles visible in Fig. 1 (j) suggest significant differences in strength, even at 550 °C. Additionally, the SEM images indicate a refinement mechanism mainly based on FeTi fragmentation, as no signs of co-deformation, e.g., significantly elongated grains in shear direction, could be observed. Such a fragmentation-based mechanism is the prevalent refinement mechanism for many soft-hard material combinations processed by HPT [30]. However, a minor degree of plastic deformation in the stronger phase cannot be excluded, especially at the highest deformation temperatures. In addition, alternative deformation modes might become important in the nanocrystalline state, especially at higher temperatures [89]. Therefore, an intrinsic convergence of strength seems to be a less plausible explanation for the enhanced refinement of FeTi at elevated temperatures.

(ii) Alloying effects and solubility

Cu exhibits only minor solubility for Fe and Ti but forms multiple intermetallic phases with the latter [90,91]. However, mechanical alloying during SPD results in a supersaturated solid solution, as reported for other material systems [30], including the Cu-Fe [92,93] and Cu–Ti systems [94,95]. Fe is one of the most efficient solutes for solid solution hardening in Cu alloys [96]. Ti imparts significant solid solution and precipitation strengthening [97], although precipitates could not be detected during this investigation, as seen in Figs. 3 and 4. As seen in

Fig. 4 (c), the lattice constant of Cu increases steadily with temperature (with significant uncertainties at 200 °C), indicating solid solution formation with up to 4 at.% Fe and 4 at.% Ti dissolving in Cu at 550 °C [98,99]. Therefore, mechanical alloying strengthens the softer Cu phase at elevated temperatures. Furthermore, the supersaturation of Cu also stabilizes its nanocrystalline state [100–102]. FeTi can accommodate some Cu in its structure, expanding the lattice [91,103]. As seen in Fig. 4 (c), the lattice constant shows a maximum at 200 °C; at higher temperatures, the lattice spacing shrinks again, converging towards the FeTi equilibrium lattice constant. Consequently, Cu substitution in FeTi has a maximum of about 8 at.% and is again lower at elevated temperatures, being about 2 at.% at 550 °C. Therefore, the solubility behaves asymmetrically when addressing higher temperatures, increasing for Cu and decreasing for FeTi, and, on average, FeTi gets dissolved in Cu. Similar results were observed in the Cu–Co system [35] and for W-transition metal composites [104], in which the fraction of the harder phase was also reduced. Due to the expanding lattices by forming solid solutions and based on the equation from Kaufman [105,106], the high pressure applied during HPT should decrease the solubility of Cu in FeTi and influence it minimally in the case of Cu. Higher temperatures can promote increased solubilities, but our work found peak solubilities at intermediate temperatures, i.e., 200 °C. The solution of Cu in FeTi also promotes the formation of Fe_2Ti, but the phase seems to be able to precipitate only at the highest deformation temperatures [91]. Consequently, the increased solubility of Cu in FeTi and vice versa can be attributed mainly to dynamic and mechanically driven processes. Overall, this mechanical alloying and partial dissolution of FeTi in Cu works in favor of extrinsic strength convergence and refinement. Nevertheless, FeTi must be refined significantly before appreciable mechanical alloying occurs. Therefore, the above alloying effects can stabilize more uniform deformation but initiate neither uniform deformation nor nanocomposite formation.

(iii) Suppression of localization by enhanced strain rate sensitivity (SRS)

High-strength materials, such as FeTi–Cu, suffer from localized deformation due to their limited ability for strain hardening. However, a high strain-rate sensitivity (SRS) can help to sustain homogeneous deformation and suppress localization phenomena [107,108]. A maximized SRS is, therefore, an essential property of high-strength materials.

Ufg Cu exhibits an increased SRS at elevated temperatures [109,110], and a similar increase was proven in the nanocrystalline regime for the fcc metals Ni and Al [111]. In this case, non-conservative dislocation processes such as climb and grain boundary interactions become significant for plastic deformation. The dominance of deformation processes involving a strong grain boundary-interaction is supported by the determined dislocation densities showing, on average, less than one dislocation per grain. One reason for this may be that dislocations are dynamically generated and absorbed at grain boundaries during deformation, leaving only few dislocations in the grain interior after deformation [79]. Also, processes not involving dislocations in the deformation process, such as grain boundary sliding, have been reported [89,112,113]. This can become more pronounced at higher temperatures [114]. Irrespective of the specific process, all of them are thermally activated and impart a significant strain rate dependence on the flow behavior, thereby increasing the SRS [79,115]. Such dislocation-mediated processes can also explain the SRS evolution in other materials, e.g., in semicrystalline polymers [116].

The more grain boundaries, the more pronounced such an effect will be. Therefore, the SRS is also inversely proportional to the Cu grain size down to the nanocrystalline regime [76,117]. These nanocrystalline states are easier to achieve and more stable in composites, with a second phase hindering recovery/recrystallization [29]. Therefore, as FeTi is refined and dispersed, Cu is also stabilized in an ufg or nanocrystalline state. Indeed, Fig. 5 shows that the CSD size of Cu processed at RT is larger than that after processing at 200 °C; the stabilization by the dispersed FeTi can explain such a trend. As discussed above, this helps to increase the SRS and develop resistance against localization.

We, therefore, deduce that at temperatures exceeding RT, the SRS of Cu becomes large enough to reduce strain localization. The thereby promoted fracture of FeTi stabilizes a smaller Cu grain size, increasing the SRS further. These concomitant effects result in a self-reinforcing refinement process that increasingly facilitates the fragmentation of FeTi by fracture and leads to the formation of the FeTi–Cu nanocomposite.

4.3. Cu-rich shear bands

Although the above effects, mechanical alloying and SRS, inhibit localization and support nanocomposite formation, Cu-rich shear bands, visible in Fig. 1 (h) and (k), were detected by SEM after deformation at 400 °C and 550 °C. The corresponding flow curves in Fig. 8 exhibit a maximum, followed by a pronounced drop in shear stress indicating softening. This might be associated with localization in the softer Cu-rich shear bands observed by SEM. Delaminated regions in Fig. 8 (c) show a Cu-like coloring, hinting at localization in the Cu-rich shear bands. Therefore, localization becomes problematic again at higher temperatures, albeit to a lower extent than at RT. Flow curves at intermediate temperatures suggest a transition temperature at around 250 °C. Above this temperature, all samples show a distinct drop in their flow curve due to the formation of Cu-rich shear bands.

The re-emergence of localization at higher temperatures could be associated with coarsening of the composite, as observed by TEM and XRD, plotted in Fig. 5, and also expected based on other studies [45,64,118,119]. A coarser structure will have a lower SRS, which might be enough to allow shear localization in Cu-rich regions [76,117]. Also, the temperature-dependent mechanical alloying strengthening the Cu phase is most pronounced at 200 °C. The reason for the reappearance of localization is therefore associated with a decline in effects (ii) and (iii) due to grain coarsening and less pronounced mechanical alloying at high deformation temperatures.

4.4. Structural heterogeneity and residual FeTi

The phenomena discussed above result in the formation of the desired nanocomposites with varying amounts of Cu-rich shear bands at elevated temperatures. As noted in Fig. 1, micrometer-sized residual FeTi particles remain dispersed in these FeTi–Cu nanocomposites. Fig. 2 (a) and (b) reveal that the amount of residual FeTi in the saturated microstructure is a function of temperature. Based on the phenomena discussed above, one can rationalize the formation of this complex microstructure as illustrated in Fig. 9.

At 200 °C, no pronounced Cu-shear bands are present in the nanocomposite. The suppression of shear bands results from effects (ii) and (iii), as seen in Figs. 4 and 5. Fig. 8 reveals a drastic strengthening, and the material becomes too hard to allow reasonable processing, even by means of HPT. The material starts to slip in between the anvils, which can be identified by sudden drops in shear stress, as indicated in Fig. 8 [72]. Even reducing the sample diameter to 6 mm, allowing pressures of up to 9.5 GPa, did not reduce this unwanted slip. Therefore, the large residual FeTi particles can be explained by the inability to introduce significantly more plastic deformation, as the uniform nanocomposite becomes simply too hard for controlled processing. If this problem could be circumvented, 200 °C might be an ideal processing window because, at this temperature, all plastic instabilities seem to be suppressed.

At temperatures higher than 250 °C, effects (ii) and (iii) become weaker, and localization in Cu-rich regions sets in, forming shear bands. Despite localization, saturation occurs along the radius of the HPT disk, and the same heterogeneous microstructure develops irrespective of strain. Figs. 2 (a) and 6 (a) depict this saturation behavior. It is concluded that the microstructural refinement, especially the fracture of

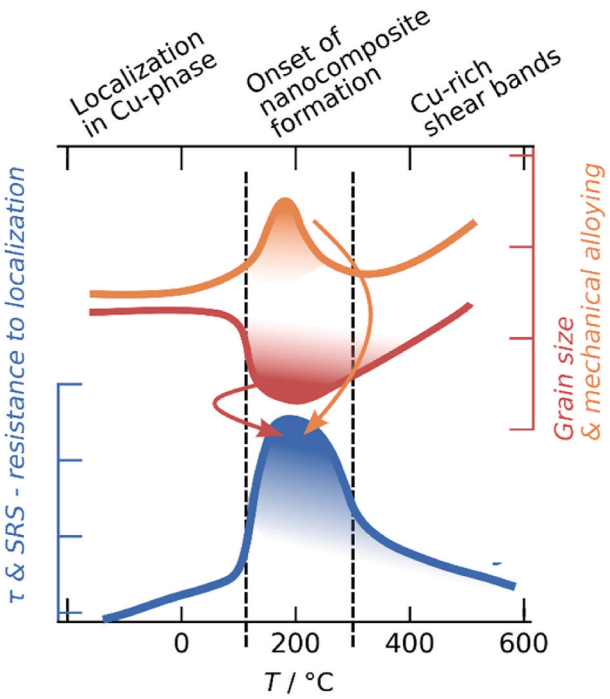

Fig. 9. Illustration of the evolution of grain refinement, mechanical alloying, and the associated resistance to deformation localization. The different microstructural regimes that result are indicated.

large, residual FeTi particles, is limited by localization in Cu-rich shear bands.

Despite this localization, refinement improves significantly when deforming at 550 °C, as reflected by Figs. 1 and 7. At 500 °C, FeTi becomes ductile, i.e., possibly undergoes a ductile-to-brittle transition [85]. The decreased fractural dimension obtained from Fig. 1 (b) indicates a different fragmentation mode and in particular a reduced resistance to fracture [60]. The increased deformability could allow easier necking and fracture of FeTi particles. Additionally, mechanical alloying could take effect as solid solution strengthening increases again for Cu at the highest temperatures but continuously diminishes for FeTi. These combined effects of enhanced ductility of FeTi and solution strengthening of Cu likely promote refinement.

5. Conclusion

Within this study, a new functional nanocomposite, FeTi-25 vol% Cu, was successfully prepared using HPT, despite difficulties due to the significant strength difference of the involved phases. By careful investigation of the resulting microstructures and the HPT process, four separate processing windows could be identified:

a) The localization is most pronounced at RT, where a continuous Cu matrix takes up most deformation, and refinement of FeTi is minimal. Thus, no desired nanocomposite forms.
b) At elevated temperatures <250 °C, a uniform FeTi–Cu nanocomposite with the highest hardness forms. The increased SRS of ufg/nc-Cu at elevated temperatures is the underlying mechanism; mechanical alloying also stabilizes uniform deformation. The enhanced refinement of FeTi supports the nc state of the Cu-phase, further increasing its SRS, resulting in a self-reinforcing refinement process.
c) At temperatures >250 °C, an FeTi–Cu nanocomposite forms, exhibiting distinct Cu-rich shear bands in which deformation is concentrated. Subsequent softening, as highlighted by a continuous drop in the flow curves, limits refinement again. The re-emergence of localization is associated with coarsening of the composite and less mechanical alloying.
d) Despite the ongoing localization, increasing the temperature as high as 550 °C results in a far improved homogeneity. The reason is the combined effect of increased deformability of the harder FeTi and well as its dissolution in the Cu phase, drastically promoting the fragmentation of FeTi.

Through this detailed study, we demonstrate that by understanding the underlying processes, even for challenging material combinations, parameters leading to the desired homogeneous nanocomposites can be identified. In the case of the FeTi–Cu, such nanocomposites could open up a viable new route for preparing superior hydrogen storage materials with well-controlled nanostructures and hydrogen sorption properties. We believe these insights will influence other research avenues so far, challenged and limited by unlikely material pairings.

Credit authors statement

Lukas Schweiger: Investigation, Formal analysis, Methodology, Visualization, Writing - Original Draft, Daniel Kiener: Conceptualization, Supervision, Validation, Writing - Review & Editing, Michael Burtscher: Investigation, Validation, Writing - Review & Editing, Erhard Schafler: Validation, Resources, Writing - Review & Editing, Gregor Mori: Conceptualization, Florian Spieckermann: Conceptualization, Supervision, Validation, Resources, Writing - Review & Editing, Jürgen Eckert: Conceptualization, Supervision, Writing - Review & Editing.

Declaration of competing interest

The authors declare that they have no known competing financial interests or personal relationships that could have appeared to influence the work reported in this paper.

Data availability

Data will be made available on request.

Acknowledgments

This research activity is part of the Strategic Core Research Area SCoRe A^+ Hydrogen and Carbon and has received funding from Montanuniversität Leoben. This research was also funded by the Austrian Science Fund (FWF) [P 34840-N]. For the purpose of open access, the author has applied a CC BY public copyright license to any Author Accepted Manuscript version arising from this submission. Furthermore, the authors acknowledge the financial support of the of the European Research Council (ERC) under the European Union's Horizon 2020 research and innovation program (Grant No. 771146 TOUGHIT).Synchrotron measurements leading to these results have been performed at PETRA III: P02.1 (I-20220565 EC) and P07 (I-20211364 EC) at DESY Hamburg (Germany) with the help of the associated beam line scientists, Alba San Jose Mendez, Martin Etter and Norbert Schell. We gratefully acknowledge the fruitful discussions with Anton Hohenwarter, Stefan Wurster, Oliver Renk, and Lukas Weissitsch, as well as the discussion with Prof. Tamas Ungar regarding the XRD evaluation.

Appendix A. Supplementary data

Supplementary data to this article can be found online at https://doi.org/10.1016/j.mtadv.2023.100433.

References

[1] R.Z. Valiev, I.V. Alexandrov, Y.T. Zhu, T.C. Lowe, Paradox of strength and ductility in metals processed bysevere plastic deformation, J. Mater. Res. 17 (2002) 5–8, https://doi.org/10.1557/JMR.2002.0002.

[2] R.Z. Valiev, Y. Estrin, Z. Horita, T.G. Langdon, M.J. Zehetbauer, Y. Zhu, Producing bulk ultrafine-grained materials by severe plastic deformation: ten years later, JOM 68 (2016) 1216–1226, https://doi.org/10.1007/s11837-016-1820-6.

[3] K. Edalati, E. Akiba, Z. Horita, High-pressure torsion for new hydrogen storage materials, Sci. Technol. Adv. Mater. 19 (2018) 185–193, https://doi.org/10.1080/14686996.2018.1435131.

[4] A. Bachmaier, R. Pippan, High-pressure torsion deformation induced phase transformations and formations: new material combinations and advanced properties, Mater. Trans. 60 (2019) 1256–1269, https://doi.org/10.2320/matertrans.MF201930.

[5] Á. Révész, M. Gajdics, High-pressure torsion of non-equilibrium hydrogen storage materials: a review, Energies 14 (2021) 819, https://doi.org/10.3390/en14040819.

[6] R.Z. Valiev, Y. Estrin, Z. Horita, T.G. Langdon, M.J. Zehetbauer, Y.T. Zhu, Fundamentals of superior properties in bulk NanoSPD materials, Mater. Res. Lett. 4 (2016) 1–21, https://doi.org/10.1080/21663831.2015.1060543.

[7] International Energy Agency, Global Hydrogen Review 2022 (2022), https://doi.org/10.1787/a15b8442-en.

[8] B.E. Lebrouhi, J.J. Djoupo, B. Lamrani, K. Benabdelaziz, T. Kousksou, Global hydrogen development - a technological and geopolitical overview, Int. J. Hydrogen Energy 47 (2022) 7016, https://doi.org/10.1016/j.ijhydene.2021.12.076. –7048.

[9] A. Odenweller, F. Ueckerdt, G.F. Nemet, M. Jensterle, G. Luderer, Probabilistic feasibility space of scaling up green hydrogen supply, Nat. Energy 7 (2022) 854–865, https://doi.org/10.1038/s41560-022-01097-4.

[10] J.A. Okolie, B.R. Patra, A. Mukherjee, S. Nanda, A.K. Dalai, J.A. Kozinski, Futuristic applications of hydrogen in energy, biorefining, aerospace, pharmaceuticals and metallurgy, Int. J. Hydrogen Energy 46 (2021) 8885–8905, https://doi.org/10.1016/j.ijhydene.2021.01.014.

[11] J. Andersson, S. Grönkvist, Large-scale storage of hydrogen, Int. J. Hydrogen Energy 44 (2019) 11901–11919, https://doi.org/10.1016/j.ijhydene.2019.03.063.

[12] N.E.F. Bloomberg, Hydrogen Economy Outlook - Key Messages, 2020. https://data.bloomberglp.com/professional/sites/24/BNEF-Hydrogen-Economy-Outlook-Key-Messages-30-Mar-2020.pdf.

[13] J.O. Abe, A.P.I. Popoola, E. Ajenifuja, O.M. Popoola, Hydrogen energy, economy and storage: review and recommendation, Int. J. Hydrogen Energy 44 (2019) 15072–15086, https://doi.org/10.1016/j.ijhydene.2019.04.068.

[14] J.J. Reilly, R.H. Wiswall, Formation and properties of iron titanium hydride, Inorg. Chem. 13 (1974) 218–222, https://doi.org/10.1021/ic50131a042.

[15] G.K. Sujan, Z. Pan, H. Li, D. Liang, N. Alam, An overview on TiFe intermetallic for solid-state hydrogen storage: microstructure, hydrogenation and fabrication processes, Crit. Rev. Solid State Mater. Sci. 45 (2020) 410–427, https://doi.org/10.1080/10408436.2019.1652143.

[16] L. Schlapbach, T. Riesterer, The activation of FeTi for hydrogen absorption, Appl. Phys. A Solids Surfaces 32 (1983) 169–182, https://doi.org/10.1007/BF00820257.

[17] L. Schlapbach, A. Züttel, Hydrogen-storage materials for mobile applications, Nature 414 (2001) 353–358, https://doi.org/10.1038/35104634.

[18] E.M. Dematteis, N. Berti, F. Cuevas, M. Latroche, M. Baricco, Substitutional effects in TiFe for hydrogen storage: a comprehensive review, Mater. Adv. 2 (2021) 2524–2560, https://doi.org/10.1039/D1MA00101A.

[19] J.R. Johnson, J. Reilly, The use of manganese substituted ferrotitanium alloys for energy storage, in: Proc. Int. Conf. Altern. Energy Sources, Upton, NY (United States), 1977, pp. 3739–3769, https://doi.org/10.2172/1004984.

[20] L. Zaluski, P. Tessier, D.H. Ryan, C.B. Doner, A. Zaluska, J.O. Ström-Olsen, M. L. Trudeau, R. Schulz, Amorphous and nanocrystalline Fe–Ti prepared by ball milling, J. Mater. Res. 8 (1993) 3059–3068, https://doi.org/10.1557/JMR.1993.3059.

[21] L. Zaluski, A. Zaluska, P. Tessier, J.O. Ström-Olsen, R. Schulz, Effects of relaxation on hydrogen absorption in Fe-Ti produced by ball-milling, J. Alloys Compd. 227 (1995) 53–57, https://doi.org/10.1016/0925-8388(95)01623-6.

[22] C.-H. Chiang, Z.-H. Chin, T.-P. Perng, Hydrogenation of TiFe by high-energy ball milling, J. Alloys Compd. 307 (2000) 259–265, https://doi.org/10.1016/S0925-8388(00)00827-6.

[23] M. Abe, T. Kuji, Hydrogen absorption of TiFe alloy synthesized by ball milling and post-annealing, J. Alloys Compd. (2007) 446–447, https://doi.org/10.1016/j.jallcom.2006.12.063, 200–203.

[24] V.Y. Zadorozhnyy, S.N. Klyamkin, S.D. Kaloshkin, Y.A. Skakov, Production of intermetallic compound of FeTi by means of mechanical-chemical synthesis and its interaction with hydrogen, Inorg. Mater. Appl. Res. 1 (2010) 41–45, https://doi.org/10.1134/S2075113310010065.

[25] A.K. Patel, D. Siemiaszko, J. Dworecka-Wójcik, M. Polański, Just shake or stir. About the simplest solution for the activation and hydrogenation of an FeTi hydrogen storage alloy, Int. J. Hydrogen Energy 47 (2022) 5361–5371, https://doi.org/10.1016/j.ijhydene.2021.11.136.

[26] K. Edalati, J. Matsuda, H. Iwaoka, S. Toh, E. Akiba, Z. Horita, High-pressure torsion of TiFe intermetallics for activation of hydrogen storage at room temperature with heterogeneous nanostructure, Int. J. Hydrogen Energy 38 (2013) 4622–4627, https://doi.org/10.1016/j.ijhydene.2013.01.185.

[27] K. Edalati, M. Matsuo, H. Emami, S. Itano, A. Alhamidi, A. Staykov, D.J. Smith, S. Orimo, E. Akiba, Z. Horita, Impact of severe plastic deformation on microstructure and hydrogen storage of titanium-iron-manganese intermetallics, Scripta Mater. 124 (2016) 108–111, https://doi.org/10.1016/j.scriptamat.2016.07.007.

[28] E.I.L. Gómez, K. Edalati, F.J. Antiqueira, D.D. Coimbrão, G. Zepon, D.R. Leiva, T. T. Ishikawa, J.M. Cubero-Sesin, W.J. Botta, Synthesis of nanostructured TiFe hydrogen storage material by mechanical alloying via high-pressure torsion, Adv. Eng. Mater. 22 (2020), 2000011, https://doi.org/10.1002/adem.202000011.

[29] A. Bachmaier, R. Pippan, Generation of metallic nanocomposites by severe plastic deformation, Int. Mater. Rev. 58 (2013) 41–62, https://doi.org/10.1179/1743280412Y.0000000003.

[30] K.S. Kormout, R. Pippan, A. Bachmaier, Deformation-Induced supersaturation in immiscible material systems during high-pressure torsion, Adv. Eng. Mater. 19 (2017), 1600675, https://doi.org/10.1002/adem.201600675.

[31] K. Edalati, H. Emami, A. Staykov, D.J. Smith, E. Akiba, Z. Horita, Formation of metastable phases in magnesium–titanium system by high-pressure torsion and their hydrogen storage performance, Acta Mater. 99 (2015) 150–156, https://doi.org/10.1016/j.actamat.2015.07.060.

[32] I. Sabirov, T. Schöberl, R. Pippan, Fabrication of a W-25%Cu nanocomposite by high pressure torsion, Mater. Sci. Forum 503–504 (2006) 561–566. https://10.4028/www.scientific.net/MSF.503-504.561.

[33] I. Sabirov, R. Pippan, Characterization of tungsten fragmentation in a W–25%Cu composite after high-pressure torsion, Mater. Char. 58 (2007) 848–853, https://doi.org/10.1016/j.matchar.2006.08.001.

[34] X. Sauvage, P. Jessner, F. Vurpillot, R. Pippan, Nanostructure and properties of a Cu–Cr composite processed by severe plastic deformation, Scripta Mater. 58 (2008) 1125–1128, https://doi.org/10.1016/j.scriptamat.2008.02.010.

[35] A. Bachmaier, J. Schmauch, H. Aboulfadl, A. Verch, C. Motz, On the process of co-deformation and phase dissolution in a hard-soft immiscible Cu Co alloy system during high-pressure torsion deformation, Acta Mater. 115 (2016) 333–346, https://doi.org/10.1016/j.actamat.2016.06.010.

[36] K.S. Kormout, P. Ghosh, A. Bachmaier, A. Hohenwarter, R. Pippan, Effect of processing temperature on the microstructural characteristics of Cu-Ag nanocomposites: from supersaturation to complete phase decomposition, Acta Mater. 154 (2018) 33–44, https://doi.org/10.1016/j.actamat.2018.05.010.

[37] K.S. Kormout, P. Ghosh, V. Maier-Kiener, R. Pippan, Deformation mechanisms during severe plastic deformation of a Cu-Ag composite, J. Alloys Compd. 695 (2017) 2285–2294, https://doi.org/10.1016/j.jallcom.2016.11.085.

[38] K. Edalati, J. Matsuda, M. Arita, T. Daio, E. Akiba, Z. Horita, Mechanism of activation of TiFe intermetallics for hydrogen storage by severe plastic deformation using high-pressure torsion, Appl. Phys. Lett. 103 (2013) 1–5, https://doi.org/10.1063/1.4823555.

[39] K. Edalati, J. Matsuda, A. Yanagida, E. Akiba, Z. Horita, Activation of TiFe for hydrogen storage by plastic deformation using groove rolling and high-pressure torsion: similarities and differences, Int. J. Hydrogen Energy 39 (2014) 15589–15594, https://doi.org/10.1016/j.ijhydene.2014.07.124.

[40] M. Zhao, I. Issa, M.J. Pfeifenberger, M. Wurmshuber, D. Kiener, Tailoring ultra-strong nanocrystalline tungsten nanofoams by reverse phase dissolution, Acta Mater. 182 (2020) 215–225, https://doi.org/10.1016/j.actamat.2019.10.030.

[41] M. Kreuzeder, M.-D. Abad, M.-M. Primorac, P. Hosemann, V. Maier, D. Kiener, Fabrication and thermo-mechanical behavior of ultra-fine porous copper, J. Mater. Sci. 50 (2015) 634–643, https://doi.org/10.1007/s10853-014-8622-4.

[42] A. Leitner, V. Maier-Kiener, J. Jeong, M.D. Abad, P. Hosemann, S.H. Oh, D. Kiener, Interface dominated mechanical properties of ultra-fine grained and nanoporous Au at elevated temperatures, Acta Mater. 121 (2016) 104–116, https://doi.org/10.1016/j.actamat.2016.08.071.

[43] M. Wurmshuber, D. Frazer, A. Bachmaier, Y. Wang, P. Hosemann, D. Kiener, Impact of interfaces on the radiation response and underlying defect recovery mechanisms in nanostructured Cu-Fe-Ag, Mater. Des. 160 (2018) 1148–1157, https://doi.org/10.1016/j.matdes.2018.11.007.

[44] M.F. Ashby, Case studies: hybrides, in: Mater. Sel. Mech. Des., Fourth, Elsevier, Burlington; US, 2011, pp. 341–366, https://doi.org/10.1016/B978-1-85617-663-7.00012-6.

[45] M. Wurmshuber, S. Doppermann, S. Wurster, D. Kiener, Ultrafine-grained tungsten by high-pressure torsion – bulk precursor versus powder processing route, IOP Conf. Ser. Mater. Sci. Eng. 580 (2019), 012051, https://doi.org/10.1088/1757-899X/580/1/012051.

[46] H.-P. Stüwe, H. Turck, Zur Messing von Fließkurven im Torsionsversuch, Int. J. Mater. Res. 55 (1964) 699–703, https://doi.org/10.1515/ijmr-1964-551107.

[47] A. Zhilyaev, G. Nurislamova, B.-K. Kim, M. Baró, J. Szpunar, T. Langdon, Experimental parameters influencing grain refinement and microstructural evolution during high-pressure torsion, Acta Mater. 51 (2003) 753–765, https://doi.org/10.1016/S1359-6454(02)00466-4.

[48] G. Ashiotis, A. Deschildre, Z. Nawaz, J.P. Wright, D. Karkoulis, F.E. Picca, J. Kieffer, The fast azimuthal integration Python library: pyFAI, J. Appl. Crystallogr. 48 (2015) 510–519, https://doi.org/10.1107/S1600576715004306.

[49] T. Ungár, Dislocation model of strain anisotropy, Powder Diffr. 23 (2008) 125–132, https://doi.org/10.1154/1.2918549.

[50] G. Williamson, W. Hall, X-ray line broadening from filed aluminium and wolfram, Acta Metall. 1 (1953) 22–31, https://doi.org/10.1016/0001-6160(53)90006-6.

[51] T. Ungár, A. Borbély, The effect of dislocation contrast on x-ray line broadening: a new approach to line profile analysis, Appl. Phys. Lett. 69 (1996) 3173–3175, https://doi.org/10.1063/1.117951.

[52] A. Newville, Matthew, Till Stensitzki, Daniel B. Allen, L.M.F.I.T. Ingargiola, Non-Linear Least-Square Minimization and Curve-Fitting for Python, 2014, https://doi.org/10.5281/zenodo.5570790.

[53] P. Virtanen, et al., SciPy 1.0: fundamental algorithms for scientific computing in Python, Nat. Methods 17 (2020) 261–272, https://doi.org/10.1038/s41592-019-0686-2.

[54] A. Borbély, The modified Williamson-Hall plot and dislocation density evaluation from diffraction peaks, Scripta Mater. 217 (2022), 114768, https://doi.org/10.1016/j.scriptamat.2022.114768.

[55] S. Berg, D. Kutra, T. Kroeger, C.N. Straehle, B.X. Kausler, C. Haubold, M. Schiegg, J. Ales, T. Beier, M. Rudy, K. Eren, J.I. Cervantes, B. Xu, F. Beuttenmueller, A. Wolny, C. Zhang, U. Koethe, F.A. Hamprecht, A. Kreshuk, ilastik: interactive machine learning for (bio)image analysis, Nat. Methods 16 (2019) 1226–1232, https://doi.org/10.1038/s41592-019-0582-9.

[56] J. Schindelin, I. Arganda-Carreras, E. Frise, V. Kaynig, M. Longair, T. Pietzsch, S. Preibisch, C. Rueden, S. Saalfeld, B. Schmid, J.-Y. Tinevez, D.J. White, V. Hartenstein, K. Eliceiri, P. Tomancak, A. Cardona, Fiji: an open-source platform for biological-image analysis, Nat. Methods 9 (2012) 676–682, https://doi.org/10.1038/nmeth.2019.

[57] J. Brocher, BioVoxxel Toolbox, 2022, https://doi.org/10.5281/zenodo.5986130.

[58] S. van der Walt, J.L. Schönberger, J. Nunez-Iglesias, F. Boulogne, J.D. Warner, N. Yager, E. Gouillart, T. Yu, scikit-image: image processing in Python, PeerJ 2 (2014) 453, https://doi.org/10.7717/peerj.453.

[59] G. Bradski, The OpenCV library, Dr, Dobb's J. Softw. Tools. 120 (2000) 122–125.

[60] D.L. Turcotte, Fractals and fragmentation, J. Geophys. Res. 91 (1986) 1921, https://doi.org/10.1029/JB091iB02p01921.

[61] W.B. Pearson, G.H. Vineyard, A handbook of lattice spacings and structures of metals and alloys, Phys. Today 11 (1958), https://doi.org/10.1063/1.3062734, 36–36.

[62] M.Y. Zadorozhnyi, S.D. Kaloshkin, S.N. Klyamkin, O.V. Bermesheva, V. Y. Zadorozhnyi, Mechanochemical synthesis of a TiFe nanocrystalline intermetallic compound and its mechanical alloying with third component, Met. Sci. Heat Treat. 54 (2013) 461–465, https://doi.org/10.1007/s11041-013-9531-x.

[63] B.B. Straumal, R. Kulagin, L. Klinger, E. Rabkin, P.B. Straumal, O.A. Kogtenkova, B. Baretzky, Structure refinement and fragmentation of precipitates under severe plastic deformation: a review, Materials 15 (2022) 601, https://doi.org/10.3390/ma15020601.

[64] R. Pippan, F. Wetscher, M. Hafok, A. Vorhauer, I. Sabirov, The limits of refinement by severe plastic deformation, Adv. Eng. Mater. 8 (2006) 1046–1056, https://doi.org/10.1002/adem.200600133.

[65] R. Pippan, S. Scheriau, A. Taylor, M. Hafok, A. Hohenwarter, A. Bachmaier, Saturation of fragmentation during severe plastic deformation, Annu. Rev. Mater. Res. 40 (2010) 319–343, https://doi.org/10.1146/annurev-matsci-070909-104445.

[66] A. Iost, R. Bigot, Indentation size effect: reality or artefact? J. Mater. Sci. 31 (1996) 3573–3577, https://doi.org/10.1007/BF00360764.

[67] E. Broitman, Indentation hardness measurements at macro-, micro-, and nanoscale: a critical overview, Tribol. Lett. 65 (2017) 1–18, https://doi.org/10.1007/s11249-016-0805-5.

[68] F. Wetscher, A. Vorhauer, R. Pippan, Strain hardening during high pressure torsion deformation, Mater. Sci. Eng. 410–411 (2005) 213–216, https://doi.org/10.1016/j.msea.2005.08.027.

[69] K. Edalati, Z. Horita, T. Furuta, S. Kuramoto, Dynamic recrystallization and recovery during high-pressure torsion: experimental evidence by torque measurement using ring specimens, Mater. Sci. Eng. 559 (2013) 506–509, https://doi.org/10.1016/j.msea.2012.08.132.

[70] M.J. Zehetbauer, J. Kohout, E. Schafler, F. Sachslehner, A. Dubravina, Plastic deformation of nickel under high hydrostatic pressure, J. Alloys Compd. 378 (2004) 329–334, https://doi.org/10.1016/j.jallcom.2004.01.039.

[71] R.B. Figueiredo, P.R. Cetlin, T.G. Langdon, Using finite element modeling to examine the flow processes in quasi-constrained high-pressure torsion, Mater. Sci. Eng. 528 (2011) 8198–8204, https://doi.org/10.1016/j.msea.2011.07.040.

[72] A. Hohenwarter, A. Bachmaier, B. Gludovatz, S. Scheriau, R. Pippan, Technical parameters affecting grain refinement by high pressure torsion, Int. J. Mater. Res. 100 (2009) 1653–1661, https://doi.org/10.3139/146.110224.

[73] A.P. Zhilyaev, S. Swaminathan, A.A. Gimazov, T.R. McNelley, T.G. Langdon, An evaluation of microstructure and microhardness in copper subjected to ultra-high strains, J. Mater. Sci. 43 (2008) 7451–7456, https://doi.org/10.1007/s10853-008-2714-y.

[74] A. Abu-Oqail, A. Wagih, A. Fathy, O. Elkady, A.M. Kabeel, Effect of high energy ball milling on strengthening of Cu-ZrO2 nanocomposites, Ceram. Int. 45 (2019) 5866–5875, https://doi.org/10.1016/j.ceramint.2018.12.053.

[75] H. Jiang, Y.T. Zhu, D.P. Butt, I.V. Alexandrov, T.C. Lowe, Microstructural evolution, microhardness and thermal stability of HPT-processed Cu, Mater. Sci. Eng. 290 (2000) 128–138, https://doi.org/10.1016/S0921-5093(00)00919-9.

[76] J. Chen, L. Lu, K. Lu, Hardness and strain rate sensitivity of nanocrystalline Cu, Scripta Mater. 54 (2006) 1913–1918, https://doi.org/10.1016/j.scriptamat.2006.02.022.

[77] V. Zadorozhnyy, S. Klyamkin, M. Zadorozhnyy, O. Bermesheva, S. Kaloshkin, Hydrogen storage nanocrystalline TiFe intermetallic compound: synthesis by mechanical alloying and compacting, Int. J. Hydrogen Energy 37 (2012) 17131–17136, https://doi.org/10.1016/j.ijhydene.2012.08.078.

[78] A. Bachmaier, J. Keckes, K.S. Kormout, R. Pippan, Supersaturation in Ag–Ni alloy by two-step high-pressure torsion processing, Phil. Mag. Lett. 94 (2014) 9–17, https://doi.org/10.1080/09500839.2013.852284.

[79] O. Renk, V. Maier-Kiener, I. Issa, J.H. Li, D. Kiener, R. Pippan, Anneal hardening and elevated temperature strain rate sensitivity of nanostructured metals: their relation to intergranular dislocation accommodation, Acta Mater. 165 (2019) 409–419, https://doi.org/10.1016/j.actamat.2018.12.002.

[80] O. Renk, A. Hohenwarter, V. Maier-Kiener, R. Pippan, Exploring the anneal hardening phenomenon in nanocrystalline Pt-Ru alloys, J. Alloys Compd. 935 (2023), 168005, https://doi.org/10.1016/j.jallcom.2022.168005.

[81] A.S. Argon, Strengthening Mechanisms in Crystal Plasticity, Oxford University Press, New York, 2007, https://doi.org/10.1093/acprof:oso/9780198516002.001.0001.

[82] R. Liang, A.S. Khan, A critical review of experimental results and constitutive models for BCC and FCC metals over a wide range of strain rates and temperatures, Int. J. Plast. 15 (1999) 963–980, https://doi.org/10.1016/S0749-6419(99)00021-2.

[83] G.Z. Voyiadjis, F.H. Abed, Microstructural based models for bcc and fcc metals with temperature and strain rate dependency, Mech. Mater. 37 (2005) 355–378, https://doi.org/10.1016/j.mechmat.2004.02.003.

[84] P.B. Hirsch, D.H. Warrington, The flow stress of aluminium and copper at high temperatures, Philos. Mag. A 6 (1961) 735–768, https://doi.org/10.1080/14786436108238367.

[85] T. Suzuki, S. Uehara, Mechanical properties of FeTi, CoTi, and NiTi at elevated temperatures, Proc. Fourth Int. Conf. Titan. 2 (1980) 1255–1264.

[86] T. Takasugi, S. Hanada, M. Yoshida, D. Shindo, A model for strength anomaly in IVa-VIII B2 ordered intermetallics, Philos. Mag. A 71 (1995) 347–358, https://doi.org/10.1080/01418619508244361.

[87] M.A. Crimp, K. Vedula, Effect of boron on the tensile properties of B2 FeAl, Mater. Sci. Eng. 78 (1986) 193–200, https://doi.org/10.1016/0025-5416(86)90323-X.

[88] Y.-W. Kim, Effects of microstructure on the deformation and fracture of γ-TiAl alloys, Mater. Sci. Eng. A. 192– 193 (1995) 519–533, https://doi.org/10.1016/0921-5093(94)03271-8.

[89] M.A. Meyers, A. Mishra, D.J. Benson, Mechanical properties of nanocrystalline materials, Prog. Mater. Sci. 51 (2006) 427–556, https://doi.org/10.1016/j.pmatsci.2005.08.003.

[90] T.B. Massalski, J.L. Murray, L.H. Bennet, Binary Alloy Phase Diagrams, ume 1, American Society for Metals, Novelty, US, 1986, https://doi.org/10.31399/asm.hb.v03.a0006247.

[91] J.A. van Beek, A.A. Kodentsov, F.J.J. van Loo, Phase equilibria in the Cu-Fe-Ti system at 1123 K, J. Alloys Compd. 217 (1995) 97–103, https://doi.org/10.1016/0925-8388(94)01302-X.

[92] X. Sauvage, R. Pippan, Nanoscaled structure of a Cu–Fe composite processed by high-pressure torsion, Mater. Sci. Eng. 410–411 (2005) 345–347, https://doi.org/10.1016/j.msea.2005.08.122.

[93] A. Bachmaier, M. Kerber, D. Setman, R. Pippan, The formation of supersaturated solid solutions in Fe–Cu alloys deformed by high-pressure torsion, Acta Mater. 60 (2012) 860–871, https://doi.org/10.1016/j.actamat.2011.10.044.

[94] C. Politis, W.L. Johnson, Preparation of amorphous Ti 1− x Cu x (0.10< x ≤0.87) by mechanical alloying, J. Appl. Phys. 60 (1986) 1147–1151, https://doi.org/10.1063/1.337359.

[95] A. Pourfereidouni, G.H. Akbari, Development of nano-structure Cu-Ti alloys by mechanical alloying process, Adv. Mater. Res. 829 (2014) 168–172. https://10.4028/www.scientific.net/AMR.829.168.

[96] H. Wendt, R. Wagner, Mechanical properties of Cu-Fe alloys in the transition from solid solution to precipitation hardening, Acta Metall. 30 (1982) 1561–1570, https://doi.org/10.1016/0001-6160(82)90176-6.

[97] S. Nagarjuna, M. Srinivas, K. Balasubramanian, D.S. Sarma, The alloy content and grain size dependence of flow stress in Cu-Ti alloys, Acta Mater. 44 (1996) 2285–2293, https://doi.org/10.1016/1359-6454(95)00358-4.

[98] J. Jiang, C. Gente, R. Bormann, Mechanical alloying in the Fe–Cu system, Mater. Sci. Eng. 242 (1998) 268–277, https://doi.org/10.1016/S0921-5093(97)00522-4.

[99] S. Nagarjuna, D.S. Sarma, On the variation of lattice parameter of Cu solid solution with solute content in Cu-Ti alloys, Scripta Mater. 41 (1999) 359–363, https://doi.org/10.1016/S1359-6462(99)00187-6.

[100] J. Weissmüller, Alloy effects in nanostructures, Nanostruct. Mater. 3 (1993) 261–272, https://doi.org/10.1016/0965-9773(93)90088-S.

[101] G. Wilde, H. Rösner, Stability aspects of bulk nanostructured metals and composites, J. Mater. Sci. 42 (2007) 1772–1781, https://doi.org/10.1007/s10853-006-0986-7.

[102] C.C. Koch, R.O. Scattergood, K.A. Darling, J.E. Semones, Stabilization of nanocrystalline grain sizes by solute additions, J. Mater. Sci. 43 (2008) 7264–7272, https://doi.org/10.1007/s10853-008-2870-0.

[103] V. Raghavan, Cu-Fe-Ti (Copper-Iron-Titanium), J. Phase Equil. 23 (2002) 172–174, https://doi.org/10.1361/1054971023604152.

[104] Z.C. Cordero, C.A. Schuh, Phase strength effects on chemical mixing in extensively deformed alloys, Acta Mater. 82 (2015) 123–136, https://doi.org/10.1016/j.actamat.2014.09.009.

[105] L. Kaufman, L. Kaufman, L. Paul, in: D.M. Warschauer (Ed.), Solids under Press, McGraw-Hill, New York, 1963, p. 303.

[106] Y. Minamino, T. Yamane, H. Araki, N. Takeuchi, Y.-S. Kang, Y. Miyamoto, T. Okamoto, Solid solubilities of manganese and titanium in aluminum at 0.1 MPa and 2.1 GPa, Metall. Trans. A 22 (1991) 783–786, https://doi.org/10.1007/BF02670301.

[107] E. Hart, Theory of the tensile test, Acta Metall. 15 (1967) 351–355, https://doi.org/10.1016/0001-6160(67)90211-8.

[108] Y.M. Wang, E. Ma, Strain hardening, strain rate sensitivity, and ductility of nanostructured metals, Mater. Sci. Eng. (2004) 375–377, https://doi.org/10.1016/j.msea.2003.10.214, 46–52.
[109] T. Suo, Y. Li, K. Xie, F. Zhao, K.-S. Zhang, Q. Deng, Experimental investigation on strain rate sensitivity of ultra-fine grained copper at elevated temperatures, Mech. Mater. 43 (2011) 111–118, https://doi.org/10.1016/j.mechmat.2011.02.002.
[110] H.W. Höppel, J. May, M. Eisenlohr, M. Göken, Strain-rate sensitivity of ultrafine-grained materials, Int. J. Mater. Res. 96 (2005) 566–571, https://doi.org/10.3139/ijmr-2005-0101.
[111] V. Maier, B. Merle, M. Göken, K. Durst, An improved long-term nanoindentation creep testing approach for studying the local deformation processes in nanocrystalline metals at room and elevated temperatures, J. Mater. Res. 28 (2013) 1177–1188, https://doi.org/10.1557/jmr.2013.39.
[112] Z. Shan, E.A. Stach, J.M.K. Wiezorek, J.A. Knapp, D.M. Follstaedt, S.X. Mao, Grain boundary-mediated plasticity in nanocrystalline nickel, Science 305 (2004) 654–657, https://doi.org/10.1126/science.1098741.
[113] H. Van Swygenhoven, P.M. Derlet, Grain-boundary sliding in nanocrystalline fcc metals, Phys. Rev. B 64 (2001), 224105, https://doi.org/10.1103/PhysRevB.64.224105.
[114] P. Ghosh, O. Renk, R. Pippan, Microtexture analysis of restoration mechanisms during high pressure torsion of pure nickel, Mater. Sci. Eng. 684 (2017) 101–109, https://doi.org/10.1016/j.msea.2016.12.032.
[115] Y. Wei, A.F. Bower, H. Gao, Enhanced strain-rate sensitivity in fcc nanocrystals due to grain-boundary diffusion and sliding, Acta Mater. 56 (2008) 1741–1752, https://doi.org/10.1016/j.actamat.2007.12.028.
[116] F. Spieckermann, H. Wilhelm, G. Polt, S. Ahzi, M. Zehetbauer, Rate mechanism and dislocation generation in high density polyethylene and other semicrystalline polymers, Polymer (Guildf) 55 (2014) 1217–1222, https://doi.org/10.1016/j.polymer.2014.01.020.
[117] A. Mishra, M. Martin, N.N. Thadhani, B.K. Kad, E.A. Kenik, M.A. Meyers, High-strain-rate response of ultra-fine-grained copper, Acta Mater. 56 (2008) 2770–2783, https://doi.org/10.1016/j.actamat.2008.02.023.
[118] O. Renk, P. Ghosh, R. Pippan, Generation of extreme grain aspect ratios in severely deformed tantalum at elevated temperatures, Scripta Mater. 137 (2017) 60–63, https://doi.org/10.1016/j.scriptamat.2017.04.024.
[119] O. Renk, R. Pippan, Transition from thermally assisted to mechanically driven boundary migration and related apparent activation energies, Scripta Mater. 154 (2018) 212–215, https://doi.org/10.1016/j.scriptamat.2018.05.052.